Cloud Timescales and Orographic Precipitation

QINGFANG JIANG* AND RONALD B. SMITH

Department of Geology and Geophysics, Yale University, New Haven, Connecticut

(Manuscript received 15 March 2001, in final form 18 October 2002)

ABSTRACT

Orographic precipitation is studied by analyzing the sensitivity of numerical simulations to variations in mountain height, width, and wind speed. The emphasis is on upslope lifting over isolated mountains in cold climates. An attempt is made to capture the essential steady-state volume-averaged cloud physics in a pair of coupled nonlinear algebraic equations. To do this, single-pathway snow formation models are analyzed with both linear and nonlinear accretion formulations.

The linear model suggests that the precipitation efficiency is determined by three timescales—the advection timescale (τ_a), fallout timescale (τ_f), and a constant timescale for snow generation (τ_{cs}). Snow generation is controlled by the ratio of τ_{cs}/τ_a and the fraction of the snow that falls to the ground is controlled by the ratio of τ_f/τ_a.

Nonlinear terms, representing accretion, reduce the utility of the timescale concept by introducing a threshold or ''bifurcation'' point, that is, a critical condensation rate that separates two states: a precipitating state and a nonprecipitating state. If the condensation rate is below the threshold value, no snow is generated. As it surpasses the threshold value, the snow generation rate increases rapidly. The threshold point is a function of advection and fallout timescales, low-level water content, mountain height, and a collection factor, which is further dependent on the geometries, terminal velocity, and density of snow particles. An approximate formula for precipitation efficiency is given in closed form.

1. Introduction

Mountain areas are natural laboratories for the study of cloud microphysics and precipitation because the dynamical forcing by mountains is relatively well defined. This is especially true for the smooth ascent situations when the atmosphere is stable and no convection occurs. For example, in the absence of convection and flow splitting, the generation rate of supersaturated water due to mountain lift can be estimated using some simple analytical models (e.g., Smith 1979). A useful index to describe the precipitation from orographic clouds is precipitation efficiency (PE), usually defined as the ratio of the total precipitation rate over a certain area to the total condensation rate. The total condensation rate is defined as the sum of condensation and deposition rates. Estimates of PE from field observations and numerical simulations vary strikingly.

Using rain gauge data collected from the windward slopes in Wales for six cases, Sawyer (1956) found that when the conditions were favorable for heavy precipitation, PE can be as high as nearly 100%. On the other hand, when the moist layer was too shallow, and less condensation occurred, PE can be reduced to 30%–50%. Elliot and Hovind (1964) estimated PE from mountains San Gabriel and Santa Ynez for 164 cases, and obtained values between 20% and 30%. They also concluded that PE tends to increase with mountain size, and is larger for convective precipitation. A case study by Browning et al. (1975) suggested that when strong, nearly saturated, moist low-level flow was directed against a mountain slope, PE can reach 70%. If the incoming flow was unsaturated, and required some finite lift to reach the lifting condensation level (LCL), PE was low (10%–30%). Young (1974a,b) simulated flow over the Front Range in Colorado from an upstream sounding. The PE estimated from his numerical simulations was 0.04% in natural conditions, and 20% with artificial seeding by silver iodide. In a series of papers concerning orographic rain on the western side of the California mountain ranges (Myers 1962; Elliot and Shaffer 1962; Colton 1976), PE values ranged from 70% to nearly 100%.

Despite the considerable variability of PE computed in previous studies, we can see some consistent correlations. The precipitation efficiency seems to depend on the moisture content of incoming flow (i.e., increase with moisture content in low-level flow), mountain size (i.e., increase with mountain size), and mountain lo-

* Current affiliation: University Corporation for Atmospheric Research, Naval Research Laboratory, Monterey, California.

Corresponding author address: Dr. Qingfang Jiang, Naval Research Laboratory, 7 Grace Hopper Ave., Monterey, CA 93943-5502. E-mail: jiang.ucar.cn@nrlmry.navy.mil

TABLE 1. Ranges of parameters.

Brunt–Väisälä frequency	$N_d = 0.011\ \text{s}^{-1}$
Wind speed	$U_0 = 10\text{–}15\ \text{m s}^{-1}$
Surface temperature	$T_0 = 270\ K$
Relative humidity	RH = 95%
Simulation time	$T = 5$ h
Mountain height	$h_m = 200\text{–}1200$ m
Mountain width	$a = 10, 30$ km
Horizontal resolution	$DX, DY = 2$ km
Vertical resolution	$Dz = 500$ m
Temporal resolution	$DT = 10$ s

cations (i.e., larger for coastal mountains). It has been argued that for a small hill, the advection timescale, that is, the time for an air parcel to drift across a mountain, might be too short for hydrometeor formation (Bergeron 1960). While the advection timescale is easily defined as the ratio of mountain width to wind speed, the timescale for hydrometeor formation is more difficult to quantify. It is not clear whether there is an inherent cloud timescale for orographic clouds.

The goal of this research is to define certain cloud timescales and establish connections between these timescales and precipitation indices such as PE. The approach takes the following steps: (i) identify the most important microphysical processes forming hydrometeors, based on the diagnosis of ARPS model runs with bulk cloud physics parameterization; (ii) develop an algebraic relationships between timescales and PE using conservation laws and a low-order box model; and (iii) compare the theoretical predictions with a large set of ARPS model runs.

To focus on cloud physics, efforts have been made to reduce the fluid-dynamical complexity of the problem. For example, neither convection nor flow splitting (Jiang 2000) is considered in this study. Our use of model output, rather than real data, is necessary at this stage to assist our search for simple mathematical formulations.

The outline of this paper is as follows. The numerical setup is described in section 2. In section 3, cloud timescales are defined based on box models. The single-pathway solutions are discussed in section 4. Theoretical results are tested against ARPS predictions in section 5. The results are summarized in section 6.

2. Numerical setup

a. ARPS model

A mesoscale model, the Advanced Regional Prediction System (ARPS), is used for this study. ARPS is a three-dimensional nonhydrostatic model developed at the Center for Analysis and Prediction of Storms (CAPS) at the University of Oklahoma. The full nonlinear momentum, continuity, and thermodynamic equations are solved on discrete grid points. The terrain-following vertical coordinate is stretched to allow higher vertical resolution in the lower troposphere. ARPS has both second- and fourth-order advection options, leapfrog time differencing and split-explicit treatment of gravity and acoustic modes, and vertically implicit options (Xue et al. 2000).

In ARPS, the ice microphysics package is based on a program developed by Tao and Simpson (1993). It includes the Kessler (1969) warm rain microphysics and a three-category ice-phase parameterization following Lin et al. (1983). There are six water categories in Lin's cloud scheme: water vapor, cloud water, rainwater, cloud ice, snow, and hail. Three of them are precipitable, that is, rainwater, snow, and hail. With the air temperature everywhere below the freezing point, little rainwater is produced in the model. Initial sensitivity tests indicated that the contribution to precipitation from hail-related processes is negligible. Hail-related processes were therefore turned off in our simulations. The only precipitable hydrometeor is snow in our research runs. Some details of the cloud parameterization scheme will be discussed in section 3.

To simplify the problem, other options, such as cumulus parameterization, surface processes, and radiation are turned off for this study.

b. Numerical setup

The topography is a 3D ideal Gaussian-type mountain specified by

$$h(x, y) = h_m \exp[-(x^2 + y^2)/a^2], \qquad (1)$$

where h_m is the maximum mountain height and a is the mountain half-width. The model domain is 103×103 with 33 vertical layers. The spatial grid sizes are $DX = DY = 2000$ m and $Dz = 500$ m. A terrain-following coordinate is used and the vertical coordinate is further stretched using a cubic function with $\delta z_{\min} = 100$ m between the lowest two layers. At $z_{\text{top}} = 12\,000$ m, the terrain-following coordinate surfaces become flat.

The model is initialized using a single sounding. The temperature profile is specified with a constant N_d, the buoyancy frequency for dry air, and a constant surface temperature T_0. For this study, we choose a surface temperature of $T_0 = 270$ K, representing typical midlatitude wintertime situations. The lapse rate is approximately 6.67 K km^{-1}. A surface temperature below the freezing point of water allows us to exclude any process related to melting layer dynamics (Marwitz 1980). The moisture is specified by a constant relative humidity. The upstream wind is unsheared and unidirectional with a wind speed U_0.

A zero gradient boundary condition is applied at the lateral boundaries. Solid wall and free-slip conditions are used at the bottom, and a solid wall condition is applied to the top boundary with Rayleigh damping near the top. The damping timescale follows Klemp and Lilly (1978).

The ranges of control parameters are listed in Table 1. With these parameters, the environmental flow is con-

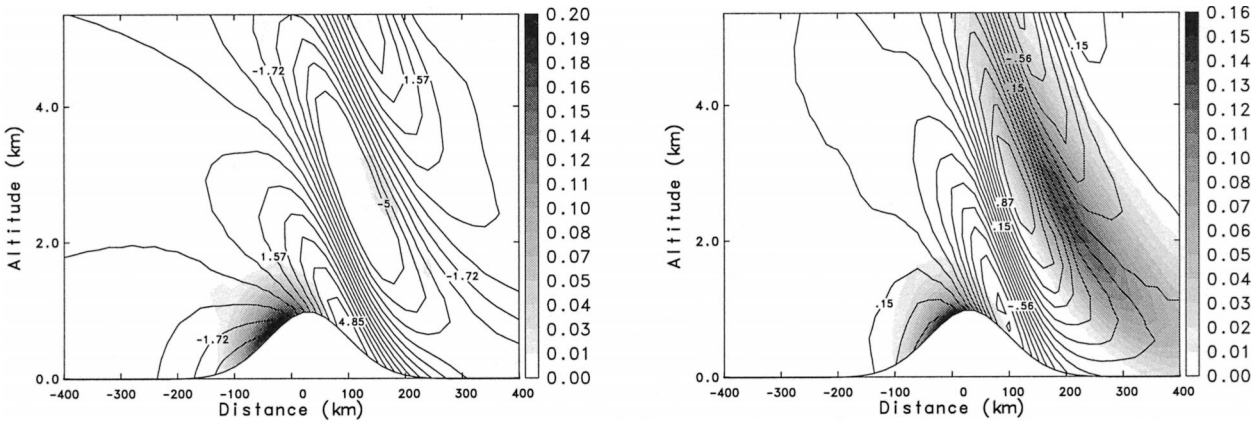

FIG. 1. Vertical cross section of the steady-state solutions through the domain center simulated by the ARPS model. The control parameters are $N_d = 0.011\ s^{-1}$, $U_0 = 10\ m\ s^{-1}$, $a = 10$ km, and $h_m = 1000$ m. (a) The perturbation horizontal velocity (m s^{-1}) is contoured (interval = 0.825) and the mixing ratio of cloud water (g kg^{-1}) is shaded (interval = 0.013); (b) vertical velocity (m s^{-1}) is contoured (interval = 0.086) and snow mixing ratio (g kg^{-1}) is shaded (interval = 0.01). Temperature is contoured (interval = 2.5°C) and cloud ice mixing ratio (g kg^{-1}) is shaded (interval = 0.01).

vectively stable, and no flow splitting occurs. As an example, the steady-state solution for $N_d = 0.011\ s^{-1}$, $U = 10\ m\ s^{-1}$, $a = 10$ km, and $h_m = 1000$ m is plotted in Fig. 1. Figure 1a shows deceleration of streamwise velocity and cloud water generation over the windward slope, and Fig. 1b shows the windward lifting and snow formation. The cloud-top temperature is about −14° to −12°C. The isotherms are rather flat with a maximum displacement less than 200 m near the hill. The windward cloud ice pattern is similar to the snow pattern (Fig. 1b) with a maximum mixing ratio of 0.05 g kg^{-1}.

3. A box model and timescale definitions

The goal of this section is to identify the most significant processes for snow production in the ARPS model and formulate the simplest possible box model equations.

a. Microphysical processes

The identification of discrete conversion processes in cold cloud microphysics is difficult at best because it requires a particle size and type classification scheme instead of treating a spectrum of sizes and habits. Wallace and Hobbs (1977) identify three processes for ice growth: growth from vapor deposition, growth by riming (i.e., accretion), and growth by aggregation. Lin has seven snow production terms: 1) collision of cloud ice to form snow, accretion of 2) cloud ice and 3) cloud water and 4) rainwater by snow, 5) vapor deposition, 6) vapor deposition associated with the Bergeron process (Bergeron 1935; Findeisen 1939), and 7) riming of cloud ice to form snow based on the growth of a 50-μm-radius ice crystal. In this context, we refer to processes 3 and 7 as riming for simplicity.

To identify the most important process(es) of snow

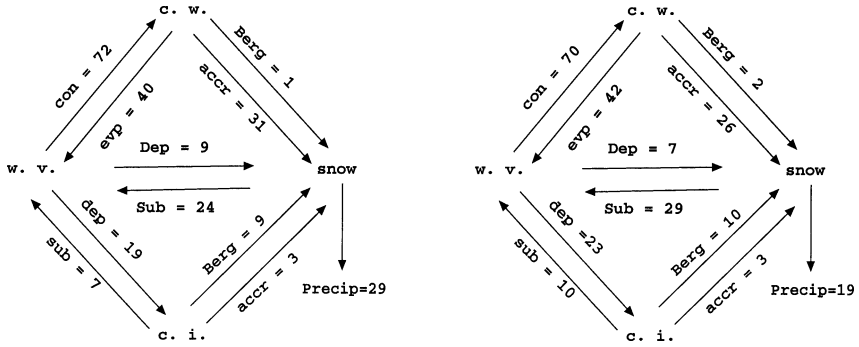

FIG. 2. Microphysical flowcharts for (a) $N_d = 0.011\ s^{-1}$, $U_0 = 10\ m\ s^{-1}$; (b) $N_d = 0.011\ s^{-1}$, $U_0 = 20\ m\ s^{-1}$; $h_m = 1000$ m and $a = 10$ km. There are four water species: water vapor (wv), cloud water (cw), cloud ice (ci), and snow. The following processes are included: condensation (con), deposition (dep), evaporation (evp), accretion (accr), riming, sublimation (sub), and precipitation (precip).

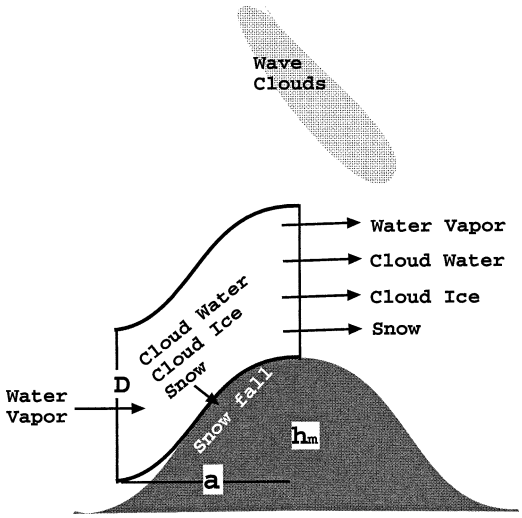

FIG. 3. Sketch of the box model. The box is three-dimensional and includes cloud water, cloud ice, and snow directly produced by mountain upslope lifting.

formation, microphysical flowcharts are created for two ARPS runs. First, the conversion rates between different water species are integrated through the control volume. Then, these rates and the total precipitation rate are scaled as a percentage of the total condensation rate. These scaled rates are labeled along with the corresponding arrows (Fig. 2). Anything less than 1% is ignored.

As seen in Fig. 2a, there are three main paths that generate snow in the model. The dominant path (hereafter, referred to as path I) is water vapor (by condensation) → supercooled cloud water (by accretion) → snow, which accounts for 60% of the total snow generation.

The second important path (hereafter, referred to as path II) is water vapor (by deposition) → cloud ice (by riming) → snow, which accounts for about 23% of the total snow generation. Direct deposition of water vapor on snow (hereafter, referred to as path III) accounts for the rest of snow production. The depositional growth rate of cloud ice and snow is mainly dependent on the supersaturation with respect to ice. In the model, this process was parameterized based on the formulation by Byers (1965) with a modified ventilation effect.

From Fig. 2b, with doubled wind speed, there are the following changes in the microphysical flowchart.

- The fractional contribution from the first path is reduced. The contribution from the second path becomes relatively more important. This change may be related to the change of the cloud-top temperature. It is known that the number density of ice nuclei (IN) is sensitive to cloud-top temperature (Rauber 1987). With a constant relative humidity, the depth of the windward clouds and therefore the cloud-top temperature is determined by dynamical parameters, U/N_d. The height and temperature of the cloud top are 1.5 km and −14°C for the run with $U_0 = 10$ m s^{-1} and 3 km and −22°C for the run with $U_0 = 20$ m s^{-1}.
- The precipitation efficiency decreases from 29% to 19% with doubled wind speed.
- The total rate of snow generation is almost unchanged (53% for both cases).
- More carryover with doubled wind speed: 45% of the snow sublimates with $U_0 = 10$ m s^{-1}, and about 56% with $U_0 = 20$ m s^{-1}.

In summary, for our setup, the most important path to produce snow in the model is water vapor (by condensation) → supercooled cloud water (by accretion) → snow. However, the relative importance of these paths may vary depending on the control parameters.

b. Box model and relevant timescales

1) BOX MODEL EQUATIONS

The box model is illustrated in Fig. 3. The box sits over the windward slope with a volume of $V = a^2D$, where D is the box height and a is a mountain width scale. Condensation, conversion, and snowfall occur in the box. Water can be carried through the box wall over the peak. Mixing ratios of water species in the box are assumed to be uniform. As wave clouds make little contribution to the total precipitation, they are not included in the box.

Based upon these assumptions, mass conversion equations can be written in terms of mixing ratios, conversion rates, and carryover rates. For the four relevant water species: water vapor, cloud water, cloud ice, and snow

$$\frac{d\hat{q}_c}{dt} = \hat{p}_{wc} - \hat{p}_{cs} - \hat{p}_{cw}, \tag{2}$$

$$\frac{d\hat{q}_i}{dt} = \hat{p}_{wi} - \hat{p}_{is} - \hat{p}_{iw}, \tag{3}$$

$$\frac{d\hat{q}_s}{dt} = \hat{p}_{cs} + \hat{p}_{is} + \hat{p}_{ws} - \hat{p}_1 - \hat{p}_{sw}, \tag{4}$$

$$\frac{d\hat{q}_w}{dt} = \hat{s} - \hat{p}_{ws} - \hat{p}_{wc} - \hat{p}_{wi}, \tag{5}$$

where $\hat{q}_c$, $\hat{q}_i$, $\hat{q}_s$, and $\hat{q}_w$ (with units of kg kg^{-1}) are the mixing ratios of cloud water, cloud ice, snow, and water vapor excess above saturation. The terms on the right-hand side [with units of kg (kg s^{-1})] are specific rates of total condensation, conversion, precipitation, and carryover. The terms $\hat{p}_{cs}$, $\hat{p}_{is}$, and $\hat{p}_{ws}$ are conversion rates to snow from cloud water, cloud ice, and water vapor, $\hat{p}_{wc}$ and $\hat{p}_{wi}$ are conversion rates from water vapor to cloud water and cloud ice, $\hat{p}_{cw}$, $\hat{p}_{iw}$, and $\hat{p}_{sw}$ represent carryover rates of cloud water, cloud ice, and snow, $\hat{p}_1$ is precipitation rate, and $\hat{s}$ is the generation rate of water vapor excess above saturation (hereafter referred to as specific total condensation rate).

2) ADVECTION TIMESCALE (τ_a)

The advection time, the time it takes for an air parcel to move across the mountain, is defined as $\tau_a = a/U_0$, where U_0 is the background wind speed. A characteristic timescale often used in box model analysis is the residence time, defined as the ratio of total mass in the box and a mass source term such as mass influx. If the total air mass in our box is Q, the influx should be $U_0(Q/a) = Q/\tau_a$. Therefore, the air residence time equals τ_a in our box model.

In this study, the advection timescale is also the time it takes for water species to travel across the control box. Therefore, along the wind direction, the rates of mass (kg s^{-1}) carried across the peak to the lee side are $\rho_a V\hat{q}_c/\tau_a$ (cloud water), $\rho_a V\hat{q}_i/\tau_a$ (cloud ice), and $\rho_a V\hat{q}_s/\tau_a$ (snow), respectively, where ρ_a is air density. For a high mountain, due to low-level blocking, both the effective mountain width and mean wind speed (near the mountain) might change.

3) TIMESCALE FOR HYDROMETEOR FALLOUT (τ_f)

Another important timescale is the time it takes for hydrometeors to fall to the ground. We define it as $\tau_f = (D + H_B)/2V_t$, where D is the height of box, H_B is cloud-base height, and V_t is the mass-weighted average falling speed. In the ARPS model, the terminal velocity of snow is proportional to $q_s^{1/16}$, that is, only weakly dependent on the mixing ratio of snow. Model output suggests that V_t varies between 1 and 2 m s^{-1}. Assuming that the bottom of the box follows streamlines, the mean downward flux of snow mass is $V\hat{q}_s/\tau_f$.

4) TIMESCALES FOR CONVERSIONS

The timescales for conversions between different water species are defined as follows. For a given water species A with mixing ratio $\hat{q}_A$ in our Eulerian control box, its mass conservation equation can be symbolically written as

$$\frac{\partial \hat{q}_A}{\partial t} = \text{Source} - \text{Sink} - \hat{p}_{AB}, \tag{6}$$

where $\hat{p}_{AB}$ is the specific conversion rate from species A to B. The corresponding conversion (from A to B) timescale is

$$\tau_{AB} = \hat{q}_A/\hat{p}_{AB} \tag{7}$$

c. Snow generation and precipitation efficiency

In steady state, the time derivatives in Eqs. (2)–(5) can be dropped. The equations can be rewritten using the cloud timescales defined in section 3b:

TABLE 2. Precipitatino indices.

Symbols	Definition
CO	Carryover factor—the ratio of snow carried over the mountain peak to the rate of snow generation CO = 1 − SPE
SGE	Snow generation efficiency—the ratio of snow generation rate to the total condensation rate ($\hat{s}$)
PE_{ww}	Windward precipitation efficiency—the ratio of windward precipitation ($\hat{p}_1$) to the total condensation rate ($\hat{s}$)
PE_{lee}	Leeside precipitation efficiency—the ratio of leeward precipitation ($\hat{p}_2$) to the total condensation rate ($\hat{s}$)
PE	Precipitation efficiency—PE = PE_{ww} + PE_{lee}
SPE	Snow precipitation efficiency—the ratio of windward precipitation to the rate of snow generation
SP	Spillover factor—the ratio of precipitation over the lee side ($\hat{p}_2$) to the total precipitation ($\hat{p}$)

$$\hat{q}_w/\tau_{wc} - \hat{q}_c/\tau_{cs} - \hat{q}_c/\tau_a = 0, \tag{8}$$

$$\hat{q}_w/\tau_{wi} - \hat{q}_i/\tau_{is} - \hat{q}_i/\tau_a = 0, \tag{9}$$

$$\hat{q}_c/\tau_{cs} + \hat{q}_i/\tau_{is} + \hat{q}_w/\tau_{ws} - \hat{q}_s/\tau_f - \hat{q}_s/\tau_a = 0, \tag{10}$$

$$\hat{s} - \hat{q}_w/(\tau_{ws}^{-1} + \tau_{wc}^{-1} + \tau_{wi}^{-1}) = 0, \tag{11}$$

where τ_{wc}, τ_{cs}, τ_{wi}, τ_{is}, τ_{ws} are timescales for conversion from water vapor to cloud water, from cloud water to snow, from water vapor to cloud ice, from cloud ice to snow, and from water vapor to snow, respectively. Based on Eqs. (8)–(11) a set of nondimensional ratio indices can be derived, describing processes in the box. The indices used in this study are listed in Table 2 for reference. Some of them are standard definitions such as windward precipitation efficiency $PE_{ww} = \hat{p}_1/\hat{s}$, and some of them have appeared in the literature, but have not been explicitly defined before, such as snow generation efficiency SGE = $(\hat{p}_{ws} + \hat{p}_{cs} + \hat{p}_{is})/\hat{s}$, and carryover CO = $\hat{p}_{sw}/(\hat{p}_{ws} + \hat{p}_{cs} + \hat{p}_{is})$.

From Eqs. (8)–(11), we obtain

$$\text{SGE} = \frac{\tau_w}{\tau_{wc}}\frac{\tau_a}{\tau_{cs} + \tau_a} + \frac{\tau_w}{\tau_{wi}}\frac{\tau_a}{\tau_{is} + \tau_a} + \frac{\tau_w}{\tau_{ws}}, \tag{12}$$

$$\text{SPE} = \frac{1}{1 + \tau_f/\tau_a}, \tag{13}$$

$$\text{CO} = \frac{1}{1 + \tau_a/\tau_f}, \tag{14}$$

$$PE_{ww} = \text{SGE} \times \text{SPE}, \tag{15}$$

where $\tau_w^{-1} = \tau_{wc}^{-1} + \tau_{wi}^{-1} + \tau_{ws}^{-1}$ is a net effective timescale for water vapor loss. Solution (12) restates the branching shown in Fig. 2 in mathematical language, in terms of cloud and advection timescales. Each ratio of a pair of timescales in Eq. (12) represents one level of branching. For example, path I (water vapor → cloud water → snow) has two steps, governed by ratios τ_w/τ_{wc} (the fraction of the saturated water vapor converted to cloud water) and $\tau_a/(\tau_{cs} + \tau_a)$ (the fraction of cloud water

converted to snow), respectively. Solutions (13)–(14) describe the branching associated with fallout and carryover. In principle, it is straightforward to generalize equations like (12)–(15) to include processes with more paths and more steps.

d. Leeside precipitation or spillover

Another important aspect of orographic precipitation is spillover, that is, precipitation over the lee slope. To predict what fraction of snow can actually fall to the ground over the lee side, one has to draw another box on the lee side. Assuming that snow carried over the peak either falls onto the lee slope or sublimates, the mass conservation equation for snow in the lee box will be

$$\frac{dq_{sl}}{dt} = \hat{p}_{sw} - \hat{p}_{\text{sub}} - \hat{p}_2, \tag{16}$$

where $\hat{p}_2 = \hat{q}_{sl}/\tau_f$ is the specific snowfall rate over the lee slope, $\hat{p}_{sw} = \hat{q}_s/\tau_a$ is snow carryover rate, $\hat{p}_{\text{sub}} = \hat{q}_{sl}/\tau_{\text{sub}}$ is the sublimation rate of snow, and $\hat{q}_{sl}$ is the snow mixing ratio in the lee box. Here τ_{sub} is the timescale for snow sublimation.

In a steady state, one can express the leeside precipitation efficiency ($\hat{p}_2/\hat{s}$) as

$$\text{PE}_{\text{lee}} = \frac{\text{PE}_{\text{ww}}}{\tau_a/\tau_f + \tau_a/\tau_{\text{sub}}}. \tag{17}$$

The total precipitation efficiency can be written as

$$\text{PE} = \text{PE}_{\text{ww}} \frac{1 + \tau_a/\tau_f + \tau_a/\tau_{\text{sub}}}{\tau_a/\tau_f + \tau_a/\tau_{\text{sub}}}. \tag{18}$$

The spillover factor (SP), the ratio of leeside precipitation and the total precipitation, can be obtained from Eqs. (17) and (18).

$$\text{SP} = \frac{1}{1 + \tau_a/\tau_f + \tau_a/\tau_{\text{sub}}} \tag{19}$$

Equation (19) shows that the spillover factor decreases with advection time, and increases with fallout time. If the mountain is wide (i.e., $\tau_a/\tau_f \gg 1$ and $\tau_a/\tau_{\text{sub}} \gg 1$), SP is small and most snow falls onto the windward slope, and if the mountain is narrow (i.e., $\tau_a/\tau_f \ll 1$ and $\tau_a/\tau_{\text{sub}} \ll 1$), most of the snow will spill over and fall on the lee side. Spillover and sublimation will be discussed in section 5b.

4. Single-pathway solutions

As shown in the previous section, precipitation indices such as PE, CO, SGE, and SP can be expressed as functions of relevant timescales. Numerical simulations suggest that typically $\tau_{wc} < 100$ s, τ_{wi}, $\tau_{ws} \sim 500$ s. Therefore, we further reduce our system (8)–(11) by assuming that $\tau_{wc} \ll \tau_{wi}$, τ_{ws}, that is, only path I is important, and the contributions from paths II and III are negligible. It should be pointed out that the timescales for physical processes and model representation of these processes can be different. In reality, condensation occurs almost instantly.

The reduced system [from Eqs. (8)–(11)] can be written as

$$\hat{s} - \hat{q}_c/\tau_{\text{init}} - \gamma \hat{q}_c \hat{q}_s^{\alpha} - \hat{q}_c/\tau_a = 0 \quad \text{(for cloud water)} \tag{20}$$

$$\hat{q}_c/\tau_{\text{init}} + \gamma \hat{q}_c \hat{q}_s^{\alpha} - \hat{q}_s/\tau_f - \hat{q}_s/\tau_a = 0 \quad \text{(for snow)}. \tag{21}$$

The conversion from cloud water to snow is written into two separate terms: $\hat{q}_c/\tau_{\text{init}}$, the linear conversion term or snow initialization term, and $\gamma \hat{q}_c \hat{q}_s^{\alpha}$, the nonlinear accretion term. The timescale of snow initialization is denoted by τ_{init} (with units of seconds) and γ (with units of inverse seconds) is referred to as a collection factor. A derivation of γ is given in appendix A.

a. Linear snow generation

If the linear snow growth process is dominant, the solution to Eqs. (20) and (21) is then

$$\hat{q}_c = \hat{s}/(\tau_{cs}^{-1} + \tau_a^{-1}), \tag{22}$$

$$\hat{q}_s = \frac{\hat{s}}{(1 + \tau_{cs}/\tau_a)(\tau_f^{-1} + \tau_a^{-1})}, \tag{23}$$

$$\text{SGE} = \frac{1}{(1 + \tau_{cs}/\tau_a)}, \tag{24}$$

$$\text{PE}_{\text{ww}} = \frac{1}{(1 + \tau_{cs}/\tau_a)(1 + \tau_f/\tau_a)}, \tag{25}$$

where $\tau_{cs} = \tau_{\text{init}} = \text{constant}$.

According to (24) and (25), if both τ_f and τ_{cs} are relatively constant, snow generation efficiency and windward precipitation efficiency (PE_{ww}) increase and carryover decreases with increasing mountain width. As an example, for $U = 10$ m s^{-1}, $\tau_f = 1000$ s, $\tau_{cs} = 1000$ s, the variation of snow generation efficiency, carryover, and precipitation efficiency with mountain width is plotted in Fig. 4.

The sensitivity of all three indices to a is strong for narrower mountains. For example, as mountain width increases from 10 to 50 km, SGE increases from 50% to 85%, PE_{ww} increases from 26% to 70%, and CO decreases from 50% to 18%. Further increasing the mountain width from 50 to 100 km, SGE increases from 85% to 91%, PE_{ww} increases from 70% to 83%, and CO decreases from 18% to 10%.

It might be instructive to look at some limits.

- The conversion is much slower than advection (i.e., $\tau_{cs} \gg \tau_a$). We have $\hat{q}_c = \tau_a \hat{s}$, SGE $= \tau_a/\tau_{cs} \to 0$, and $\text{PE}_{\text{ww}} \to 0$. This is the situation when the mountain is too narrow and the advection timescale is too short for hydrometeor formation and precipitation. Hence, all the condensed water is carried over the peak and evaporates. No snow is generated and therefore no

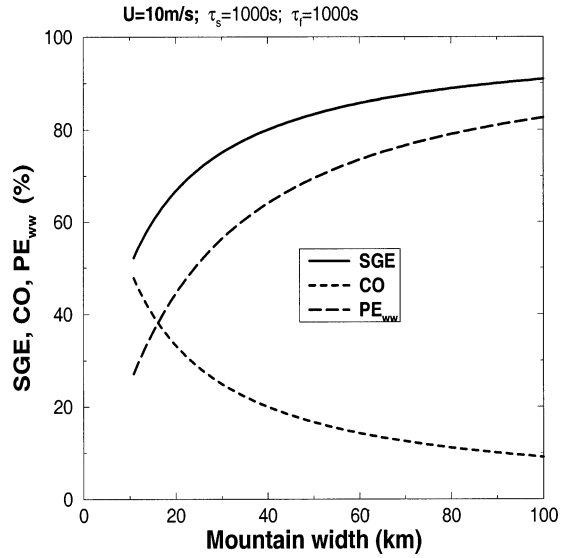

FIG. 4. Linear box model solutions. SGE (24), CO (14), and PE_{ww} (25) vs mountain width. Wind speed $U = 10$ m s^{-1}, fallout time $\tau_f = 1000$ s, and conversion time $\tau_{cs} = 1000$ s.

precipitation occurs. The cloud water $\hat{q}_c$ is only a function of mountain lift (i.e., h_m), and independent of wind speed. This is the classical nonprecipitating scenario as moist flow crosses a narrow mountain.

- Both the conversion and falling of snow are much faster than advection (i.e., τ_{cs}, $\tau_f \ll \tau_a$). We have $\hat{q}_c = \hat{s}\tau_{cs}$, $\hat{q}_s = \hat{s}\tau_f$, $PE_{ww} \to 1$, SGE $\to 1$ and CO $\to 0$. In this limit, the advection time is so long that virtually all the condensed water is converted to snow, and all the snow precipitates. This could happen as moist flow passes a wide mountain, especially with proper number density of ice nuclei or seeding from high clouds.
- The conversion is much faster and the falling is much slower than advection (i.e., $\tau_{cs} \ll \tau_a \ll \tau_f$). We have $\hat{q}_s = \hat{s}\tau_a$, SGE $\to 1$, CO $\to 1$, and PE $\to 0$. The conversion from cloud water to snow is so fast that most of the condensed water is converted to snow. However, the falling of snow particles is so slow that virtually all snow particles are carried over to the lee side, and there is no precipitation over the windward slope. This could be true if moist air with overpopulated ice nuclei hits a relatively wide mountain. The growing of snow is fast enough, but particles are too small to fall to the ground.

b. Nonlinear accretion

The box model with linear snow generation allows us to connect precipitation efficiency with a constant cloud timescale τ_{cs} and the advection timescale τ_a in a very simple form. However, the importance of nonlinear accretion in snow formation has been well established (Cotton 1986; Cotton and Anthes 1989; Pruppacher and Klett 1997), and generally used in cloud parameterization. This basic aspect of microphysical parameterization is so fundamental that it needs be included even in simplified models.

For $\alpha = 1$ and ignoring the snow initialization term, one can solve Eqs. (20) and (21) for $\hat{q}_c$, $\hat{q}_s$, and PE_{ww}. One set of solutions is $\hat{q}_s = 0$, $\hat{q}_c = \hat{s}\tau_a$, and $PE_{ww} = 0$, that is, no snow is produced and all the condensed water evaporates over the lee slope. The other set of solutions is

$$\hat{q}_c = \gamma^{-1}(\tau_f^{-1} + \tau_a^{-1}), \tag{26}$$

$$\hat{q}_s = \frac{\hat{s}}{\tau_a^{-1} + \tau_f^{-1}} - \gamma^{-1}\tau_a^{-1}, \tag{27}$$

$$PE_{ww} = \left(1 - \frac{\tau_a^{-1} + \tau_f^{-1}}{\gamma\tau_a\hat{s}}\right)\frac{1}{1 + \tau_f/\tau_a}. \tag{28}$$

Based on Eqs. (27) and (28), we can define a critical specific total condensation rate, $\hat{s}_c$,

$$\hat{s}_c = \frac{\tau_a^{-1} + \tau_f^{-1}}{\gamma\tau_a}. \tag{29}$$

If $\hat{s} < \hat{s}_c$, both $\hat{q}_s$ and PE_{ww} are negative. It is unphysical to have negative snow, and it cannot occur in the ARPS model either, because all the water species are explicitly forced to be nonnegative (Xue et al. 1995). Therefore, we have to piece the two roots together. For $\hat{s} < \hat{s}_c$, we have $\hat{q}_c = \hat{s}\tau_a$, $\hat{q}_s = 0$, and $PE_{ww} = 0$, and for $\hat{s} > \hat{s}_c$, we have Eqs. (26)–(28) with snow formation and precipitation. In other words, $\hat{s} = \hat{s}_c$ is a threshold point that separates the system into two states: a nonprecipitating state ($\hat{s} < \hat{s}_c$; $\hat{q}_s = 0$) and a precipitating state ($\hat{s} > \hat{s}_c$; $\hat{q}_s > 0$).

Defining a nondimensional specific total condensation rate $R = \hat{s}/\hat{s}_c$, solutions (26)–(28) can be rewritten as

$$\hat{q}_c = \frac{\hat{s}\tau_a}{R} = \hat{s}_c\tau_a, \tag{30}$$

$$\hat{q}_s = \frac{R - 1}{\gamma\tau_a}, \tag{31}$$

$$\text{SGE} = 1 - 1/R, \tag{32}$$

$$PE_{ww} = \frac{1 - 1/R}{1 + \tau_f/\tau_a}. \tag{33}$$

For $R > 1$, the timescale for conversion from cloud water to snow is

$$\tau_{cs} = \frac{\tau_a}{R - 1}. \tag{34}$$

In (30)–(34), the nondimensional specific total condensation rate (R) is critical to the cloud timescale, snow formation, and precipitation.

The variation of PE_{ww} with R is plotted in Fig. 5a. It shows a rapid increase of PE_{ww} as R increases from 1 to about 3. As R becomes larger, PE_{ww} increases with R at a slower pace. The reason for PE_{ww} increasing with

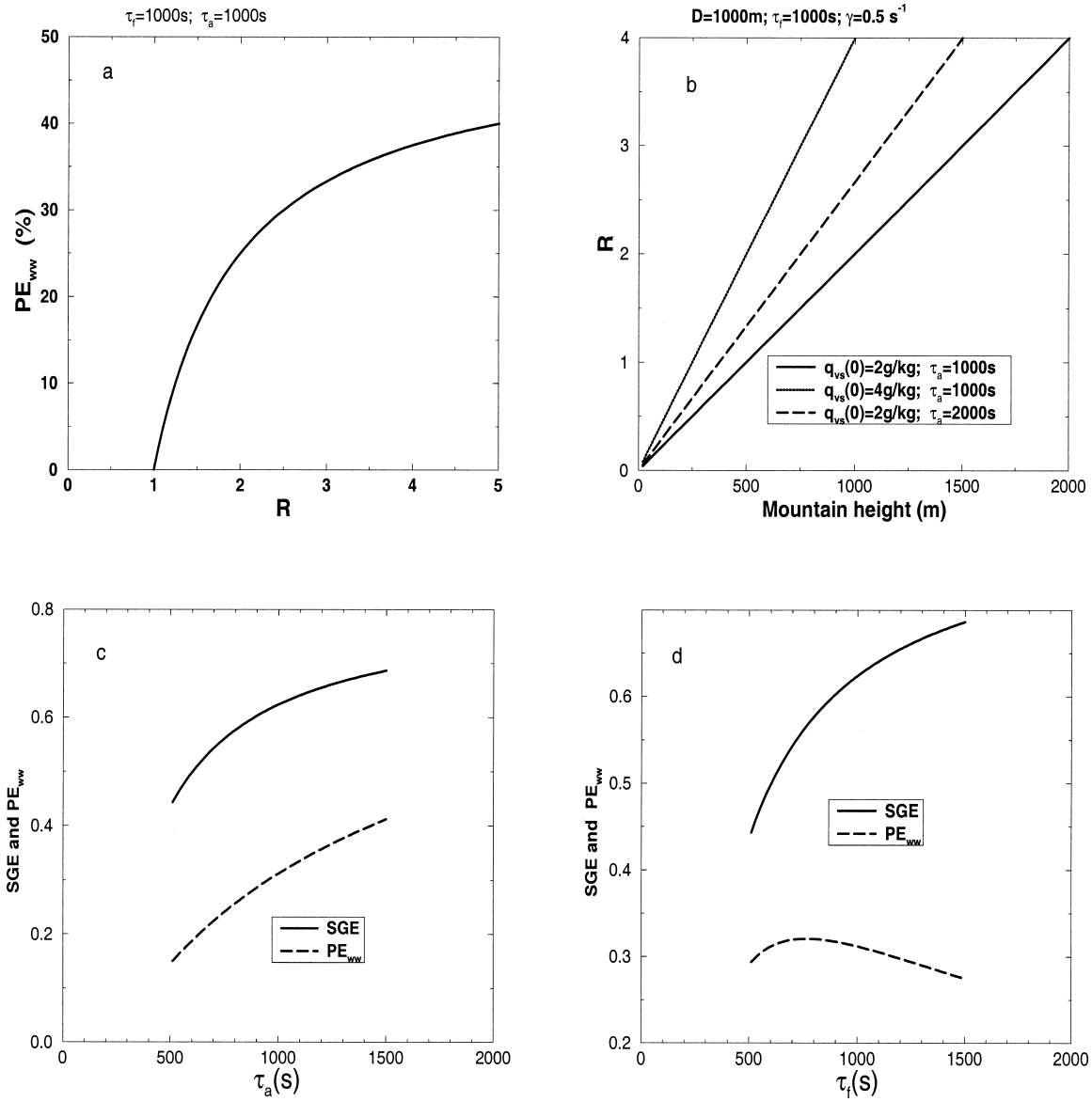

FIG. 5. Nonlinear solutions. (a) PE_{ww} (33) vs R for $\tau_a = \tau_f = 1000$ s. (b) The nondimensional specific total condensation rate R vs mountain height h_m (37) for $H = 1000$ m, $\tau_f = 1000$ s, $\gamma = 0.5$ s^{-1}. Three curves correspond to the following sets of parameters: q_{vs} (0) = 2 g kg^{-1} and $\tau_a = 1000$ s (solid); q_{vs} (0) = 4 g kg^{-1} and $\tau_a = 1000$ s (dotted); and q_{vs} (0) = 2 g kg^{-1} and $\tau_a = 2000$ s (dashed). (c) SGE and PE_{ww} [(32), (33)] vs advection timescale τ_a. (d) SGE and PW_{ww} [(32), (33)] vs fallout timescale τ_f.

R can be seen clearly from Eq. (34). The nondimensional conversion time (i.e., the ratio of τ_{cs} and τ_a) decreases from ∞ to 1 as R increases from 1 to 2. This strong nonlinearity is associated with the nonlinear accretion formulation.

The occurrence of threshold behavior in solutions (31)–(33) is quite interesting. It has become a common practice to parameterize some microphysical processes with specified threshold points in cloud physics schemes (Lin et al. 1983; Schultz 1995, among others). Unlike these models with explicitly built-in threshold points, our threshold point is introduced by the nonlinearity of the accretion.

The threshold point separates the solution into two distinct states: a precipitating state and a nonprecipitating state. The nonprecipitating state is characterized by few snow crystals, little accretion, long conversion timescale, and low snow generation efficiency. The precipitating state is characterized by abundant snow crystals, fast accretion, short conversion timescale, and high snow generation efficiency. The mathematical and physical basis of the threshold point (i.e., $R = 1$) will be

TABLE 3. Box model solutions.

Indices	Linear conversion	Nonlinear accretion	
SGE	$\frac{1}{1+\tau_{cs}/\tau_a}$	$1-\frac{1}{R}$	$(R>1)$
PE_{ww}	$\frac{1}{(1+\tau_{cs}/\tau_a)(1+\tau_f/\tau_a)}$	$\frac{1-1/R}{1+\tau_f/\tau_a}$	$(R>1)$
CO	$\frac{1}{1+\tau_a/\tau_f}$	$\frac{1}{1+\tau_a/\tau_f}$	
SPE	$\frac{1}{1+\tau_f/\tau_a}$	$\frac{1}{1+\tau_f/\tau_a}$	
PE_{lee}	$\frac{1}{(1+\tau_{cs}/\tau_a)(1+\tau_a/\tau_f)(1+\tau_f/\tau_{sub})}$	$\frac{1-1/R}{(1+\tau_a/\tau_f)(1+\tau_f/\tau_{sub})}$	$(R>1)$
SP	$\frac{1+\tau_f/\tau_a}{(1+\tau_f/\tau_a)+(1+\tau_a/\tau_f)(1+\tau_f/\tau_{sub})}$	$\frac{1+\tau_f/\tau_a}{(1+\tau_f/\tau_a)+(1+\tau_a/\tau_f)(1+\tau_f/\tau_{sub})}$	
PE	$PE_{ww}+PE_{lee}$	$PE_{ww}+PE_{lee}$	

further examined in the following sections. Both solutions to the linear and nonlinear box models are listed in Table 3 for reference.

c. *The nondimensional specific total condensation rate R*

To further examine the physical implication of R, we estimate $\hat{s}$ using the slab model described by Smith (1979). Assuming that the incoming air is saturated, the environmental temperature $T(z)$ lies along a moist adiabat, and flow at all levels is parallel to the sloping mountain surface [i.e., the vertical motion $w(z) = w(0) = U_0 h_x$, where h_x is the terrain slope], the vertically integrated total condensation rate over a unit horizontal area is

$$\int_0^\infty w\left.\frac{dq_{vs}}{dz}\right|_{ad} dz = \rho_{a0} q_{vs}(0) U_0 h_x, \tag{35}$$

where ρ_{a0} and $q_{vs}(0)$ are air density and saturation mixing ratio of water vapor at the ground. For an axisymmetric Gaussian mountain, the specific total condensation rate can be obtained by integrating Eq. (35) over the windward slope and divided by the reference volume of the box V,

$$\hat{s} = \frac{\sqrt{\pi} q_{vs}(0) h_m U_0}{Da}. \tag{36}$$

As an example, for $h_m = 1000$ m, $a = 10$ km, $U_0 = 10$ m s^{-1}, $\rho_{a0} = 1.2$ kg m^{-3}, and $q_{vs}(0) = 10^{-3}$ kg kg^{-1}, we obtain $\hat{s} = 3.4 \times 10^{-3}$ g (kg s)$^{-1}$. Using (29) and (36), we have

$$R = \gamma \frac{\sqrt{\pi} q_{vs}(0) h_m}{D(\tau_a^{-1} + \tau_f^{-1})} \tag{37}$$

As an example, the variation of R with mountain height, water content, and advection time (37) is plotted in Fig. 5b. For $D = 1$ km, $\tau_f = 1000$ s, $\gamma = 0.5$ s^{-1}, $\tau_a = 1000$ s, $q_{vs}(0) = 2$ g kg^{-1}, the critical mountain height to have $R = 1$ is roughly 500 m. The critical mountain height reduces to 375 m for a mountain twice as wide and reduces to 250 m if the water vapor content $q_{vs}(0)$ is doubled.

Mathematically, to change from a nonprecipitating state to a precipitating state, one has to increase R, either

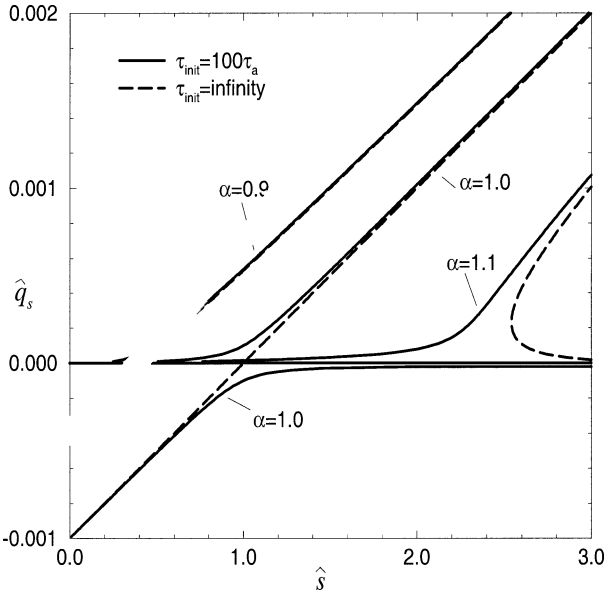

FIG. 6. Snow mixing ratio ($\hat{q}_s$) vs the specific total condensation rate ($\hat{s}$). Solutions to Eqs. (20)–(21) with nonlinear accretion. Three set of solutions are plotted: $\alpha = 1$ with $\tau_{init} = 100\tau_a, \infty$; $\alpha = 0.9$ with $\tau_{init} = 100\tau_a, \infty$; and $\alpha = 1.1$ with $\tau_{init} = 100\tau_a, \infty$. Nonphysical roots for the $\alpha = 1$ case are shown as negative numbers. Nonphysical roots for $\alpha \neq 1$ are complex.

by increasing the specific total condensation rate $\hat{s}$, or decreasing the critical specific total condensation rate $\hat{s}_c$. Based on Eq. (37), this can be achieved in several ways.

- Here R can be increased by the increase of dynamical factors such as mountain height h_m, water vapor content $q_{vs}(0)$, and advection time τ_a. The increase of h_m or $q_{vs}(0)$ increases cloud water supply $\hat{s}$, accelerates the accretion process, and increases the snow generation efficiency. This positive feedback process can be symbolically expressed as $[q_{vs}(0), h_m] \uparrow\rightarrow (\hat{s}, R) \uparrow\rightarrow$ Accr $\uparrow\rightarrow$ SGE $\uparrow$. In the linear interpretation, increasing τ_a gives more time for conversion, $\tau_a \uparrow\rightarrow$ Accr $\uparrow\rightarrow$ SGE $\uparrow$. In the nonlinear interpretation, increasing τ_a decreases $\hat{s}_c$ (29), thereby increasing SGE (32). A larger τ_a also reduces the fraction of snow drifting to the lee side (e.g., Fig. 5c).
- Additionally, R can be increased by the increase of microphysical factors such as the collection factor (γ) or the fallout time τ_f. Increasing γ or τ_f decreases $\hat{s}_c$ (29), which accelerates the accretion process. Symbolically, we have, $(\gamma, \tau_f) \uparrow\rightarrow R \uparrow\rightarrow$ Accr $\uparrow\rightarrow$ SGE $\uparrow$ (e.g., Fig. 5d). However, it should be pointed out that, as shown in appendix A, γ and τ_f are related through the falling speed V_T.

In summary, the box model with nonlinear accretion suggests that both snow generation efficiency and precipitation efficiency are controlled by the nondimensional specific total condensation rate (R). The faster the saturation, the more condensed water is converted to snow and falls to the ground. This result agrees qualitatively with observations. Previous studies suggested that a decreased moisture content can lead to a decreased precipitation efficiency (Sawyer 1956; Browning et al. 1974), and precipitation efficiency also tends to increase with mountain size (Elliot and Hovind 1964).

d. The mathematics and physics of the threshold point

The mathematical nature of the threshold point needs to be further studied. First, there are two solutions to Eqs. (20) and (21) when $\alpha = 1$, that cross at $\hat{s} = \hat{s}_c$. In the previous discussion, we simply pieced the two solutions together. If we believe that our box model is a reasonable representation of the physical system, we have to justify our choice of roots. Why is $\hat{q}_s = 0$ not appropriate for $\hat{s} > \hat{s}_c$? Second, is the threshold point a unique feature for $\alpha = 1$? As we do not know the precise value of α in the laboratory or in nature, if the threshold behavior exists only for $\alpha = 1$, it will not be very interesting physically.

To answer the first question, we re-solve Eqs. (20) and (21) with both the snow initialization and nonlinear accretion terms (with $\alpha = 1$):

$$\hat{q}_s = \frac{\hat{s} - \gamma^{-1}(\tau_a^{-1} + \tau_f^{-1})(\tau_a^{-1} + \tau_{\text{init}}^{-1}) \pm \{[\gamma^{-1}(\tau_a^{-1} + \tau_f^{-1})(\tau_a^{-1} + \tau_{\text{init}}^{-1}) - \hat{s}]^2 + 4\tau_{\text{init}}^{-1}\gamma^{-1}\hat{s}(\tau_a^{-1} + \tau_f^{-1})\}^{1/2}}{2(\tau_a^{-1} + \tau_f^{-1})}. \tag{38}$$

By retaining the snow initialization term we regularize Eqs. (20) and (21), allowing us to see how the threshold behavior develops. The pair of roots in (38) are plotted in Fig. 6 as a function of $\hat{s}$. The addition of the small snow initiation term shifts the $\hat{q}_s = 0$ root slightly. For $\hat{s} < \hat{s}_c$, the $\hat{q}_s = 0$ root becomes slightly positive. For $\hat{s} > \hat{s}_c$, the $\hat{q}_s = 0$ root becomes negative and thus is unphysical.

The snow initialization term slightly smooths the threshold but retains its basic character. The threshold point becomes $\hat{s}_c = (\tau_a^{-1} + \tau_f^{-1})(\tau_a^{-1} + \tau_{\text{init}}^{-1})/\gamma$. For $\hat{s} < \hat{s}_c$, $\hat{q}_s$ increases with $\hat{s}$ very slowly. For $\hat{s} \geq \hat{s}_c$, the physical root starts to increase with $\hat{s}$ rapidly.

To answer the second question, solutions to (20) and (21) are determined numerically for various values of α. Four solutions are plotted in Fig. 6 corresponding to $\alpha = 0.9$, $\tau_{\text{init}} = \infty$, $100\tau_a$ and $\alpha = 1.1$, $\tau_{\text{init}} = \infty$, $100\tau_a$ respectively. For $\alpha = 0.9$, the threshold is not as sharp as when $\alpha = 1$. The additional smoothing effect of the snow initialization term is barely seen. For $\alpha = 1.1$ and $\tau_{\text{init}} = \infty$, the threshold changes its character. Two positive roots are seen. Again we can regularize the equation with a reasonably large τ_{init}. The threshold point is smoothed and shifted, but still well defined.

Therefore, we can conclude that the threshold behavior of the box model solution, associated with the nonlinearity of the accretion term, is robust. It exists at least for a range of α near unity, in the presence of a small linear ''initialization'' term. The threshold behavior in the orographic precipitation problem arises from the positive feedback process involving snow generation. The higher the snow amount, the faster the rate of snow generation. Such a process would run away if it were not limited by a finite rate of cloud water generation. For $\hat{s} < \hat{s}_c$, the supply rate is not large enough to sustain the feedback loop at all. For $\hat{s} > \hat{s}_c$, a steady-state snow generation can be sustained without exhausting the cloud water supply.

There are several mathematical analogies to this threshold behavior. Perhaps the simplest is the Euler buckling of a beam. This phenomenon can be illustrated by pressing on the ends of a plastic or metal ruler with

force F. When F is less than F_{crit}, no bending occurs. When F slightly exceeds F_{crit}, the ruler takes on a bend with amplitude proportional to the square root of the quantity $(F - F_{\text{crit}})$ (e.g., Gilmore 1981); a response curve similar to Fig. 5a. Another example of bifurcation is Rayleigh–Bénard convection (Malkus and Veronis 1958). If the Rayleigh number (Ra) exceeds R_{crit}, the amplitude of the motion rises in a way similar to Fig. 5a. A third physical system with a response curve like Fig. 5a is the density change of a Van der Waals gas through a critical point, a so-called second-order phase transition.

There is a general feeling in the microphysical community that thresholds may arise from a triggering process involving small inputs. For example, a small addition of ice nuclei could cause ice multiplication to begin. Sparse preexisting ice in an air mass could have large effect. Cloud seeding is based on such an idea. In contrast, the threshold in our model has a different origin. It is more closely related to the ability of bulk processes to maintain themselves. In fact, we illustrated that small seeding terms have little influence in our model. The analogies mentioned earlier are of similar origin to ours. The Euler buckling does not depend upon faults or nicks in the beam. The onset of cellular convection does not depend on tiny ''hot spots'' or imperfections on the lower boundary. Both of these bifurcations, and ours in this paper, arise from the instability and nonlinearity of the bulk processes.

5. Diagnosis of the ARPS model

In the previous sections, two versions of a box model are investigated: linear snow generation and nonlinear accretion. The two models make very different predictions of PE_{ww}. In this section, we will compare the box model predictions against ARPS model runs with bulk cloud physics. For comparison, three groups of runs have been carried out with $N_d = 0.011\ \text{s}^{-1}$, $T_0 = 270$ K, RH = 0.95. Mountain height varies from 200 to 1200 m, mountain width varies from 10 to 30 km, and wind speed from 5 to 30 m s^{-1}. The corresponding indices are evaluated from ARPS output using volume-averaged quantities. For example, $\hat{q}_s = \int_V \rho_a q_s\, dV / \int_V \rho_a\, dV$, in which the control volume V includes the space over the windward slope wherever the local snow mixing ratio q_s is nonzero. The volume-averaged specific conversion rates can be defined similarly. For example, the conversion rate from cloud water to snow $\hat{p}_{cs}$ is $\int_V \rho_a p_{cs}\, dV / \int_V \rho_a\, dV$.

a. The effect of mountain height

Because change of mountain height does not change the timescales for advection and snow fallout, the linear conversion model predicts that both the precipitation efficiency and snow generation efficiency are independent of the mountain height [(24), (25)]. However, the nonlinear accretion model suggests that both the precipitation efficiency and snow generation efficiency increase strongly with the mountain height [(32), (33), (37)]. For example, increasing mountain height from 600 to 1200 m, the snow generation efficiency increases from 35% to 70% (Fig. 7a), and precipitation efficiency increases from 22% to 36% (Fig. 7c). The ARPS model agrees with the accretion model in the sense that both quantities increase with the mountain height. Compared with the accretion model, the ARPS increase is more moderate. Doubling the mountain height from 600 to 1200 m, the snow generation efficiency from the ARPS model increases from 35% to 58% (Fig. 7a).

Both the ARPS model and the box model with nonlinear accretion seem to follow the causality chain: the higher mountain → more supersaturated water → faster conversion → higher precipitation and snow generation efficiency. This mechanism is also supported by previous studies. For example, Elliot and Hovind (1964) concluded that precipitation efficiency tends to increase with mountain size. Assuming that the incoming flow is always convectively stable, and the mountain lift is identical, we should be able to create a similar causality chain for humidity variation, that is, higher humidity → more supersaturated water → faster conversion → higher precipitation and snow generation efficiency. The increase of precipitation efficiency with humidity is found in previous studies (Sawyer 1956; Browning et al. 1974) as well.

Based on the box model (both linear and nonlinear), the carryover factor is only a function of advection and snow fallout timescales (see Table 3), independent of the mountain height. The ARPS model suggests a slow decrease of carryover with increasing mountain height; a 2% decrease over the range of mountain height from 600 to 1200 m (Fig. 7b). A plausible explanation is that as the mountain height increases, the low-level flow blocking shifts the maximum lift toward the upstream, which increases the real mountain width.

Based on the variations of precipitation efficiency and snow generation efficiency, it seems that the threshold point predicted by the nonlinear accretion model is not well supported by ARPS simulations (Fig. 7a). However, if one computes the snow generation efficiency using the production rate of snow by the first path alone and the total condensation rate (Fig. 7a), a threshold point can be clearly seen near $h_m \sim 200$–300 m. It seems that when the mountain height and $\hat{s}$ are small, the second and third paths become more important. It should be pointed out that although three processes (i.e., conversion from cloud water to rainwater, conversion from cloud ice to snow, and accretion of snow particles to form hail) were formulated with explicit threshold points in Lin's scheme, none of them are relevant to the first path (water vapor → cloud water → snow).

The spillover factor is more difficult to evaluate due to the complexity in estimating τ_{sub}, the sublimation timescale. Presumably, the speed of sublimation is con-

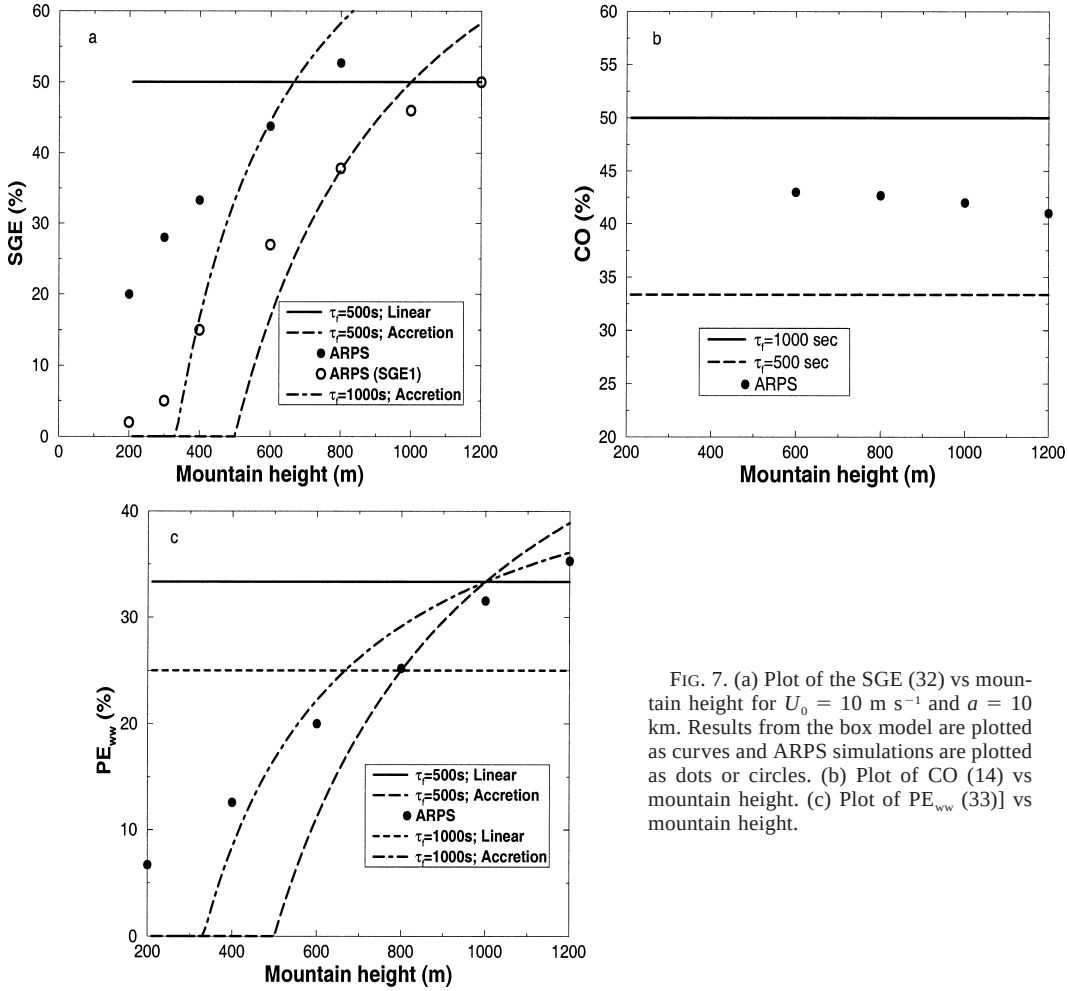

FIG. 7. (a) Plot of the SGE (32) vs mountain height for $U_0 = 10$ m s^{-1} and $a = 10$ km. Results from the box model are plotted as curves and ARPS simulations are plotted as dots or circles. (b) Plot of CO (14) vs mountain height. (c) Plot of PE_{ww} (33)] vs mountain height.

trolled by two processes—the drying of the air associated with flow descent and the microphysical sublimation of snow particles in an unsaturated environment. The diagnosis of model output seems to suggest that flow descent is the dominant factor. For a simple estimation, we assume

$$\tau_{\text{sub}} = H_s/\hat{w}, \tag{39}$$

where H_s is a ''scale height'' of snow sublimation that presumably depends on mountain height and moisture stratification; and $\hat{w}$ is the averaged speed of downdraft, which can be estimated as the product of the mean wind speed and the average slope of the terrain, that is, $\hat{w} = U_0 h_m/a$. Therefore, we obtain

$$\text{SP} = \frac{1}{1 + \tau_a/\tau_f + h_m/H_s}. \tag{40}$$

The comparison of Eq. (40) with $H_s = 1$ km and the ARPS simulation is shown in Fig. 8. The spillover factor decreases with increasing mountain height, which agrees with Eq. (40). However, the spillover factor predicted by the leeside box model decreases with increasing mountain height more slowly than the ARPS prediction. A plausible reason is that the maximum lift over the windward slope migrates upstream as the mountain height increases due to stronger nonlinearity. This migration increases the effective across-mountain width (i.e., a), and decreases CO (as suggested by Fig. 7b), which further reduces the spillover factor.

b. The effect of wind speed

Previous studies suggested that strong low-level wind helps to enhance orographic precipitation. A simple interpretation is that the slope-induced vertical velocity and the total condensation rate are proportional to the wind speed. The more subtle and important question is how the precipitation efficiency changes with wind speed.

Both ARPS runs and the box model suggest that snow generation efficiency decreases with wind speed (Fig. 9a). In the box models, the decrease of SGE with wind speed is solely due to the decrease of advection timescale [(24), (32), (37)]. The linear box

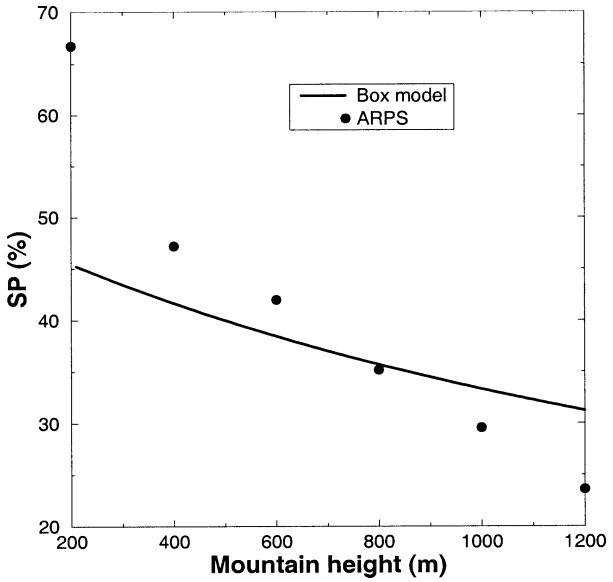

FIG. 8. Plot of SP vs mountain height for $U_0 = 10$ m s^{-1} and $a = 10$ km. The solid curve is from the box model (40) with $H_s = 1$ km. ARPS simulations are plotted as points.

model predicts a stronger decrease than the nonlinear accretion box model for $U_0 < 24$ m s^{-1} and slower decrease for $U_0 > 24$ m s^{-1} with $\tau_f = 1000$ s (Fig. 9a). The decrease predicted by ARPS is slower than that by the box model, in general, presumably due to the increasing importance of the second and third paths ignored in the box model.

The carryover factor shows a strong increase with wind speed, due to the shortened advection timescales (Fig. 9b). As $U_0 = 10$ m s^{-1}, about 40% of the snow spills over and as wind speed doubles, the spillover percentage increases to about 55%. The accretion mechanism does not play any role in the computation of the carryover factor. The ARPS runs fall in between $\tau_f = 500$ s and $\tau_f = 1000$ s, which suggests that ARPS runs should have an equivalent τ_f somewhere around 750 s.

The total precipitation efficiency shows a strong decrease with increasing wind speed (Fig. 9c). As wind speed doubles from 10 to 20 m s^{-1}, the corresponding precipitation efficiency decreases from 27% to 18%. However, if the assumption that the total condensation

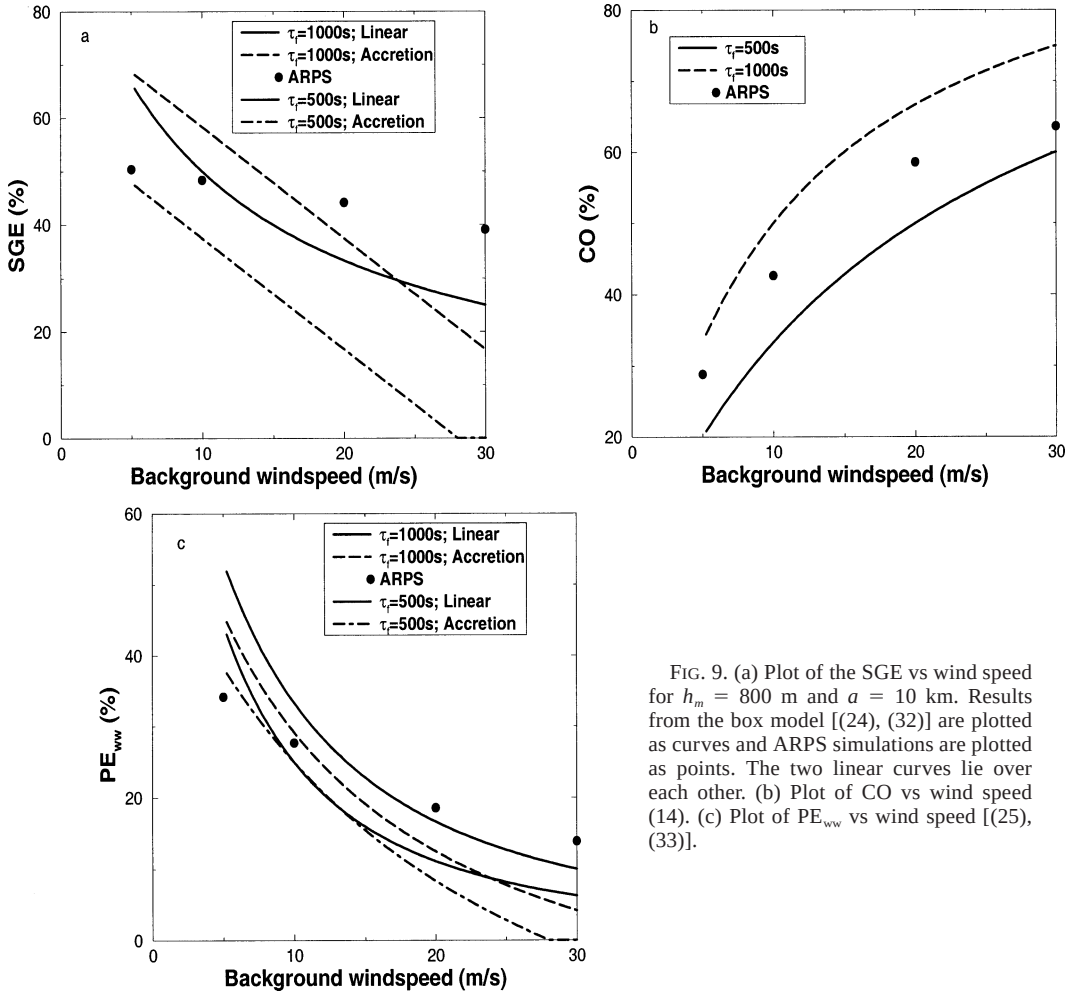

FIG. 9. (a) Plot of the SGE vs wind speed for $h_m = 800$ m and $a = 10$ km. Results from the box model [(24), (32)] are plotted as curves and ARPS simulations are plotted as points. The two linear curves lie over each other. (b) Plot of CO vs wind speed (14). (c) Plot of PE_{ww} vs wind speed [(25), (33)].

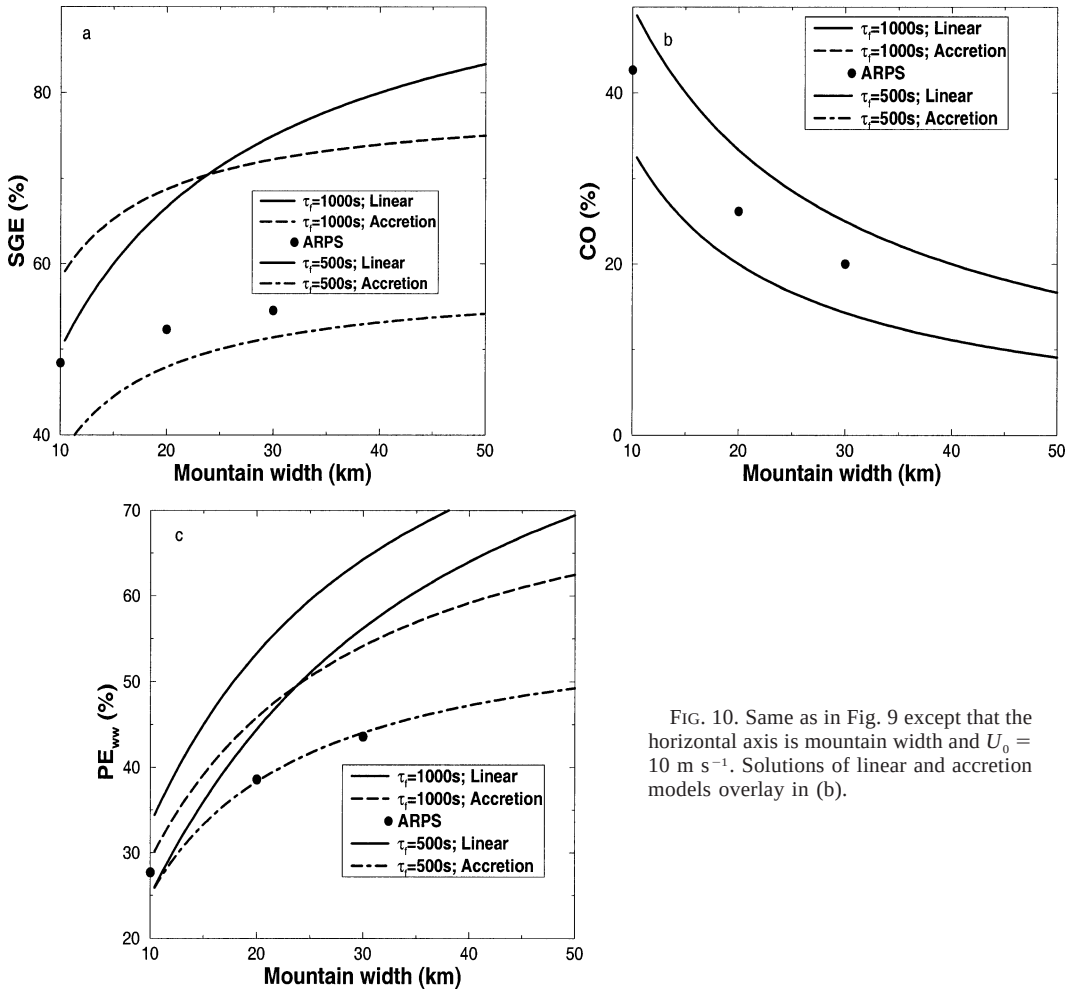

FIG. 10. Same as in Fig. 9 except that the horizontal axis is mountain width and U_0 = 10 m s^{-1}. Solutions of linear and accretion models overlay in (b).

rate is proportional to wind speed is right, the total precipitation rate over the mountain should still increase about 30%. Therefore, this study suggests that the total precipitation increases with wind speed at a pace much slower than proportionality.

c. The effect of mountain width

Corresponding to the increase of the mountain width from 10 to 30 km, the increases of snow generation efficiency predicted by the nonlinear accretion box model, the linear conversion box model, and the ARPS model are 14%, 25%, and 7%, respectively (Fig. 10a). The slower increase predicted by the nonlinear accretion model than the linear conversion model is consistent with the variation of the average snow mixing ratio. As the mountain becomes wider, the slope decreases, and the average mixing ratios of snow and cloud water decrease too.

The decrease in the average snow mixing ratio results in a longer conversion time, which slows down the increase of snow generation efficiency. All the models indicate roughly a 20% decrease of carryover, upon increasing the mountain width from 10 to 30 km (Fig. 10b). With a tripling of the mountain width, all the models predict a moderate increase of precipitation efficiency (nonlinear accretion model, 23%; linear conversion model, 32%; and ARPS model, 16%). The agreement between the nonlinear accretion model and the ARPS is especially encouraging (Fig. 10c). According to the nonlinear accretion box model, as the mountain width is further increased from 30 to 50 km, precipitation efficiency only increases an additional 7%.

The increase of precipitation efficiency with mountain width agrees with previous studies, and also is consistent with conventional wisdom that a wider mountain gives a longer time for hydrometeor formation and precipitation. However, our results also suggest that an increase of mountain width will decrease the average mixing ratio of snow and cloud water, and slow down snow formation. This effect increases the conversion timescale and slows the rise in snow generation efficiency and precipitation efficiency. Our results also suggest that precipitation efficiency increases with mountain width more rapidly for narrower mountains.

6. Conclusions

To summarize this paper, we revisit the question we asked at the beginning: Can we define an inherent (constant) cloud timescale that helps us to understand orographic precipitation features such as precipitation efficiency and spillover?

The plausible answer seems to be no. There is no such characteristic timescale for hydrometeor formation. A fixed timescale would imply linearity in the microphysical conversion process, but nonlinear accretion processes are critical to the growth of hydrometeors. Therefore, the timescale for snow formation varies with incoming flow condition (such as water vapor content, stability, and wind speed), the terrain features (such as mountain height and cross-mountain width), and microphysical details (such as density, habit, and size of snow particles).

The concept of cloud timescales, however, still promises to be useful for understanding orographic precipitation. The highly simplified box model allows us to connect the precipitation features (such as snow generation efficiency, carryover, precipitation efficiency, and spillover factor) to relevant timescales. This formulation offers a consistent description of the variation of these indices with incoming flow and terrain features.

Some of our results only confirm conventional wisdom. For example, precipitation efficiency should increase with increasing mountain width because the advection timescale—the time allowed for hydrometeor formation and precipitation—increases. While the box model supports this argument, it provides us some new insight as well. The box model suggests that increasing mountain width does increase the snow generation efficiency and precipitation efficiency. However, increasing the mountain width decreases the slope and, therefore, decreases the specific total condensation rate $\hat{s}$. This negative effect slows down the accretion processes, and increases the timescale for snow formation. As a result, the snow generation efficiency increases with mountain width only slightly. The increase of precipitation efficiency is largely due to the decrease of carryover, that is, more precipitation and less carryover.

Our new results include the threshold point and the increase of precipitation efficiency with water content and mountain height. It has been suspected for years that some microphysical processes have threshold behavior. Therefore, threshold points are widely used in cloud parameterizations. Unlike these schemes with empirical threshold points, the threshold point in the box model is produced by the nonlinearity of the accretion processes and the rapid depletion of cloud water by snow. We demonstrated how the sharp distinction between precipitating and nonprecipitating clouds can be described with a pair of nonlinear algebraic equations [(20), (21)] and their solutions. The nondimensional specific total condensation rate R is the key factor in determining precipitation efficiency. An approximate formula for R is given by (37). The box model formulation predicts that precipitation efficiency increases with both water content and mountain height, by accelerating accretion and decreasing the conversion timescale.

As demonstrated, the agreement between the ARPS runs and the algebraic box model formulas is encouraging. The variation of precipitation efficiency, snow generation efficiency, and carryover with mountain size and wind speed can be qualitatively understood in terms of advection, snow fallout, and cloud timescales.

On the other hand, it is important to bear in mind that the box model and timescale argument are based on a considerable simplification. Hence, we will revisit our assumptions to highlight some of the limitations of the results.

First, our incoming flow is always stable, and no convection occurs. Once convection occurs, we should expect new timescales, perhaps unrelated to mountain forcing. Our box model and timescale analysis are no longer directly applicable. Previous studies indicated that convection might increase precipitation efficiency.

Second, the incoming flow is uniform, no frontal system or large-scale weather pattern is considered. Previous observations suggested that orogenic precipitation (precipitation induced solely by mountains) is rare, and most of the studied cases were characterized by orographic enhancement (of the large-scale precipitation). However, if the large-scale stratiform precipitation is weak and widespread, the falling hydrometeors play two roles: evaporating to moisten the low-level flow, and seeding the orographic clouds. Under such conditions, our conclusions should be applicable.

Third, in this study, the nondimensional mountain height is relatively small, so that we are in the dynamical ''flow over'' regime. Low-level flow blocking and flow splitting will change the effective mountain width (a), mountain lift ($\hat{s}$), and cloud volume (V). Hence our results cannot directly apply to such situations. Some modifications are necessary.

Fourth, it is known that precipitation is very sensitive to cloud-top temperature (Rauber 1987). For colder clouds the production of ice crystals at cloud top will reduce the amount of cloud water and strongly modify these results. With a constant RH, the cloud-top level is controlled by dynamical parameters such as wind speed and stability. Simulations have been done (not shown) with less stable air. Results suggest that the windward clouds are higher, cloud-top temperature is lower, more ice crystals are produced, and the precipitation is greater. Further systematic studies are required to quantify the influence of cloud-top temperature on PE and test our analytical formulations.

Finally, we are well aware that this study seeks only to reconcile model results. It cannot identify or correct errors in microphysical formulations. Although bulk cloud parameterizations have been tested in numerous case studies, some important processes not considered

in current parameterizations can influence precipitation efficiency. For example, precipitation efficiency can be increased by slow drizzle precipitation and ground vegetation, which removes cloud water near the ground. Precipitation efficiency can be different for continental and maritime air masses even under identical conditions of wind, stratification, humidity, temperature, and topography due to condensation nuclei or ice nuclei differences.

While the gap between our idealized study and the real world is obvious, the concepts developed in this paper may help to improve our understanding of orographic clouds and precipitation. The connection between nonlinear microphysics and increasing PE might also be applicable to warm clouds and to nonorographic clouds. If the nonlinearity is common, it would provide a negative feedback on water vapor concentration in the atmosphere.

Acknowledgments. The authors thank Dr. Vanda Grubisic and three anonymous reviewers for their constructive comments and suggestions. This research was supported by the National Science Foundation Division of Atmospheric Sciences (ATM-9711076). The simulations were made using the Advanced Regional Prediction (ARPS) developed by the Center for Analysis and Prediction of Storms (CAPS), University of Oklahoma. CAPS is supported by the National Science Foundation and the Federal Aviation Administration. The computing was done on an SGI Origin 200 at the Yale Center for Earth Observation.

APPENDIX A

Collection Factor γ

To compare with ARPS, we still need to determine the collection factor γ for the nonlinear accretion model. Assuming that the number density of cloud water and snow particles are n_c (m^{-3}) and n_s (m^{-3}), respectively, and m_c and m_s are mass of a cloud or snow particle, the collection rate of cloud water mass CR (kg m^{-3} s^{-1}) is

$$\mathrm{CR} = (AV_T n_s) n_c m_c, \tag{A1}$$

where A (m^2) is the average intercept area of snow particles, and V_T is the vertical velocity of snow particles.

Using $\hat{q}_s = m_s n_s/\rho_a$, $\hat{q}_c = m_c n_c/\rho_a$, where $\rho_a = 1.2$ kg m^{-3} is the air density, we obtain

$$\frac{\mathrm{CR}}{\rho_a} = (A\rho_a V_T)\frac{\hat{q}_s \hat{q}_c}{m_s}, \tag{A2}$$

which gives

$$\gamma = \frac{\rho_a A V_T}{m_s}. \tag{A3}$$

Assuming the snow particles to be spheres of radius R_s, we have

$$m_s = \frac{4\pi}{3}\rho_s R_s^3, \tag{A4}$$

where ρ_s is snow density. Using Eq. (A4) and $A = \pi R_s^2$, we obtain

$$\gamma = \frac{3\rho_a V_T}{4\rho_s R_s}, \tag{A5}$$

which suggests that γ is at least a function of the habit, density, size, and terminal velocity of snow particles. Physically, the quantity γ is the rate at which falling particles sweep out air (in kg) divided by the particle mass (in kg).

As an example, for $R_s = 0.45$ cm, $V_T = 1.0$ m s^{-1}, and $\rho_s = 100$ kg m^{-3}, we obtain $\gamma = 2$ s^{-1}.

APPENDIX B

List of Symbols

Symbol	Description
a	Mountain half-width (km)
h_m	Max mountain height (m)
U_0	Incoming wind speed (m s^{-1})
T_0	Ground temp (K)
RH	Relative humidity (%)
N_d	Dry buoyancy frequency (s^{-1})
τ_a	Advection timescale (s)
τ_f	Fallout timescale (s)
τ_{cs}	Conversion timescale from cloud water to snow (s)
τ_{sub}	Leeside sublimation timescale (s)
τ_{wc}	Condensation timescale (s)
τ_{wi}	Timescale for deposition of water vapor to cloud ice (s)
τ_{ws}	Timescale for deposition of water vapor to snow (s)
τ_{is}	Timescale for conversion from cloud ice to snow (s)
$\hat{q}_w$	Mixing ratio of water vapor in the box (kg kg^{-1})
$\hat{q}_c$	Mixing ratio of cloud water in the box (kg kg^{-1})
$\hat{q}_i$	Mixing ratio of cloud ice in the box (kg kg^{-1})
$\hat{q}_s$	Mixing ratio of snow in the box (kg kg^{-1})
$\hat{s}$	Specific total condensation rate [kg (kg s)$^{-1}$]
R	Nondimensional specific total condensation rate
V	Volume of the box (m^3)
D	Cloud depth (m)
H_B	Cloud-base height (m)
H_s	Scale height of snow sublimation
γ	Collection factor (1/s)
τ_{init}	Snow initialization timescale (s)
$q_{vs}(0)$	Water vapor saturation mixing ratio at the ground (kg kg^{-1})
$\hat{p}_{wc}$	Specific condensation rate in the box [kg (kg s)$^{-1}$]

$\hat{p}_{wi}$ Specific deposition rate of water vapor to cloud ice in the box [kg (kg s)$^{-1}$]
$\hat{p}_{ws}$ Specific deposition rate of water vapor to snow in the box [kg (kg s)$^{-1}$]
$\hat{p}_{cs}$ Specific conversion rate from cloud water to snow in the box [kg (kg s)$^{-1}$]
$\hat{p}_{is}$ Specific conversion rate from cloud ice to snow in the box [kg (kg s)$^{-1}$]
$\hat{p}_{1}$ Specific precipitation rate over windward slope [kg (kg s)$^{-1}$]
$\hat{p}_{cw}$ Specific rate of cloud water carried out of the box to lee side [kg (kg s)$^{-1}$]
$\hat{p}_{iw}$ Specific rate of cloud ice carried out of the box to lee side [kg (kg s)$^{-1}$]
$\hat{p}_{sw}$ Specific rate of snow carried out of the box to lee side [kg (kg s)$^{-1}$]
$\hat{p}_{2}$ Specific precipitation rate over lee side [kg (kg s)$^{-1}$]

REFERENCES

Bergeron, T., 1935: On the physics of cloud and precipitation. *Proc. Fifth Assembly of the Int. Union of Geodesy and Geophysics,* Lisbon, Portugal, IUGG, 156–178.

——, 1960: Problems and methods of rainfall investigation. *Physics of Precipitation, Geophys. Monogr.,* No. 5, Amer. Geophys. Union, 5–30.

Browning, K. A., F. F. Hill, and C. W. Pardoe, 1974: Structure and mechanism of precipitation and the effect of orography in a wintertime sector. *Quart. J. Roy. Meteor. Soc.,* **100,** 309–330.

——, C. Pardoe, and F. F. Hill, 1975: The nature of orographic rain at wintertime cold fronts. *Quart. J. Roy. Meteor. Soc.,* **101,** 333–352.

Byers, H. R., 1965: *Elements of Cloud Physics.* The University of Chicago Press, 191 pp.

Colton, D. E., 1976: Numerical simulation of the orographically induced precipitation distribution for use in hydrologic analysis. *J. Appl. Meteor.,* **15,** 1241–1251.

Cotton, W. R., 1986: Numerical simulation of the effects of varying ice crystal nucleation rates and accretion processes on orographic snowfall. *J. Climate Appl. Meteor.,* **25,** 1658–1680.

——, and R. A. Anthes, 1989: *Storm and Cloud Dynamics.* Academic Press, 883 pp.

Elliot, R. D., and R. W. Shaffer, 1962: The development of quantitative relationships between orographic precipitation and airmass parameters for use in forecasting and cloud seeding evaluation. *J. Appl. Meteor.,* **1,** 218–228.

——, and E. L. Hovind, 1964: The water balance of orographic clouds. *J. Appl. Meteor.,* **3,** 235–239.

Findeisen, W., 1939: The evaporation of cloud and raindrops. *Z. Meteor.,* **56,** 453–460.

Gilmore, B., 1981: Catastrophe theory for scientists and engineers. John Wiley and Sons, 666 pp.

Jiang, Q., 2000: Some theoretical aspects of orographic precipitation. Ph.D. thesis, Yale University, 144 pp.

Kessler, E., 1969: *On the Distribution and Continuity of Water Substance in Atmospheric Circulations. Meteor. Monogr.,* No. 32, Amer. Meteor. Soc., 84 pp.

Klemp, J. B., and D. K. Lilly, 1978: Numerical simulations of hydrostatic mountain waves. *J. Atmos. Sci.,* **35,** 78–107.

Lin, Y. L., R. D. Farley, and H. D. Orville, 1983: Bulk parameterization of the snow field in a cloud model. *J. Climate Appl. Meteor.,* **22,** 1065–1092.

Malkus, W. V. R., and G. Veronis, 1958: Finite amplitude cellular convection. *J. Fluid Mech.,* **4,** 225–260.

Marwitz, J., 1980: Winter storms over the San Juan Mountains. Part I: Dynamical processes. *J. Appl. Meteor.,* **19,** 913–926.

Myers, V. A., 1962: Airflow on the windward side of a ridge. *J. Geophys. Res.,* **67,** 4267–4291.

Pruppacher, H. R., and J. D. Klett, 1997: *Microphysics of Clouds and Precipitation.* Kluwer Academic, 954 pp.

Rauber, R. M., 1987: Characteristics of cloud ice and precipitation during wintertime storms over the mountains of northern Colorado. *J. Climate Appl. Meteor.,* **26,** 488–524.

Sawyer, J. S., 1956: The physical and dynamical problems of orographic rain. *Weather,* **11,** 375–381.

Schultz, P., 1995: An explicit cloud physics parameterization for operational numerical weather prediction. *Mon. Wea. Rev.,* **123,** 3331–3343.

Smith, R. B., 1979: The influence of mountains on the atmosphere. *Advances in Geophysics,* Vol. 21, Academic Press, 87–230.

Tao, W. K., and J. Simpson, 1993: Goddard Cumulus Ensemble Model. Part I: Model description. *Terr. Atmos. Oceanic Sci.,* **4,** 35–72.

Wallace, J. M., and P. V. Hobbs, 1977: *Atmospheric Sciences.* Academic Press, 467 pp.

Xue, M., K. K. Droegemeier, V. Wong, A. Shapiro, and K. Brewster, 1995: ARPS Version 4.0 User's Guide. Center for Analysis and Prediction of Storms, 380 pp.

——, ——, and ——, 2000: The Advanced Regional Prediction System (ARPS)—A multiscale nonhydrostatic atmospheric simulation and prediction model. Part I: Model dynamics and verification. *Meteor. Atmos. Physics,* **75,** 161–193.

Young, K. C., 1974a: A numerical simulation of wintertime, orographic precipitation: Part I. Description of model microphysics and numerical techniques. *J. Atmos. Sci.,* **31,** 1735–1748.

——, 1974b: A numerical simulation of wintertime, orographic precipitation: Part II. Comparison of natural and AgI-seeded conditions. *J. Atmos. Sci.,* **31,** 1749–1767.